Article | Open Access

Energy Materials

Liu *et al. Energy Mater.* **2026**, *6*, 600103 **DOI:**10.20517/energymater.2026.98

Trace Mn doping activates ZIF-67 through reconstruction to Co-Mn (oxy)hydroxides for enhanced oxygen evolution

Deyou Liu[1,2,#], Hanwen Luan[3,#], Hongjie Guo[1], Yongqiang Li[2], Ningning Shao[2], Roberto Boada[3], Zhijun Dong[2], Hongliang Li[1,*], Xiang-Yang Lou[2,*], Zhijie Chen[4]

Keywords:
Oxygen evolution reaction, metal-organic frameworks, electrochemical reconstruction, Mn-Co bimetallic catalysts, seawater splitting

Citation: Liu, D.; Luan, H.; Guo, H.; Li, Y.; Shao, N.; Boada, R.; Dong, Z.; Li, H.; Lou, X. Y.; Chen, Z. Trace Mn doping activates ZIF-67 through reconstruction to Co-Mn (oxy)hydroxides for enhanced oxygen evolution. *Energy Mater.* **2026**, *6*, 600103. https://dx.doi.org/10.20517/energymater.2026.98

Received: 30 Apr 2026
First Decision: 12 Jun 2026
Revised: 17 Jul 2026
Accepted: 6 Aug 2026
Published: 25 Aug 2026

Academic Editor:
Yuhui Chen
Copy Editor:
Shu-Yuan Duan
Production Editor:
Shu-Yuan Duan

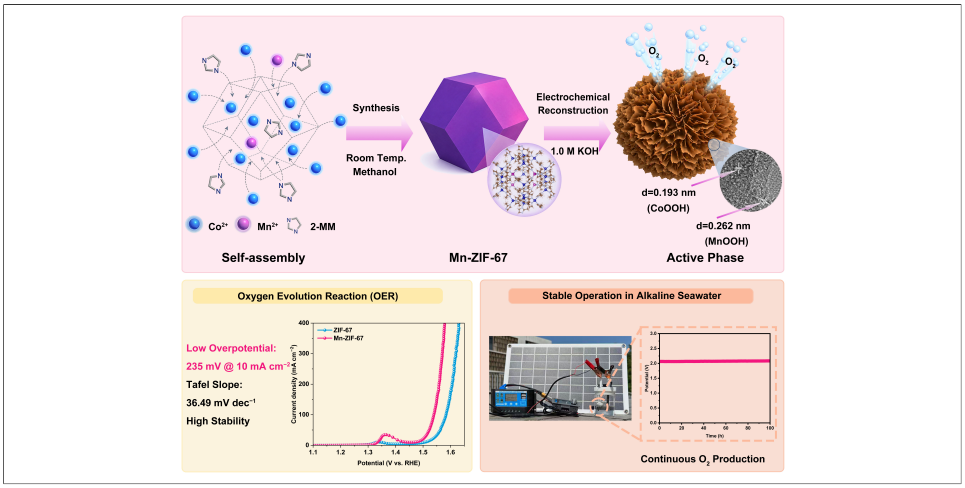

Abstract

Understanding how trace-metal doping directs the electrochemical reconstruction of MOF precatalysts into the true active phase remains a key challenge in designing efficient oxygen evolution reaction (OER) electrocatalysts. Here, a bimetallic Mn-Co zeolitic imidazolate framework-67 material, denoted as Mn-ZIF-67, was prepared through a facile room-temperature self-assembly route that incorporated trace Mn into the ZIF-67 lattice. Compared with undoped ZIF-67, Mn-ZIF-67 exhibits enhanced alkaline OER performance, with the overpotential at 10 mA cm^{-2} (η_{10}) value decreasing from 276 to 235 mV, a reduced Tafel slope of 36.49 mV dec^{-1}, and sustained stability during long-term durability testing. A combination of structural characterization and density functional theory (DFT) calculations demonstrates that Mn-ZIF-67 undergoes electrochemical surface reconstruction into Mn-modified Co (oxy)hydroxides, which serve as the real catalytically active phase. Mn-mediated electronic modulation optimizes intermediate adsorption energetics and lowers

[1]College of Mining Engineering, Taiyuan University of Technology, Taiyuan 030024, Shanxi, China.
[2]Institute of Technology for Future Industry (School of Science and Technology Instrument Application Engineering), Shenzhen University of Information Technology, Shenzhen 518172, Guangdong, China.
[3]GTS-UAB Research Group, Department of Chemistry, Facultat de Ciències, Universitat Autònoma de Barcelona, Bellaterra 08193, Spain.
[4]UNSW Water Research Centre, School of Civil and Environmental Engineering, University of New South Wales, Sydney 2052, Australia.
[#]These authors contributed equally to this work.

[*]**Correspondence to:** Prof. Hongliang Li, College of Mining Engineering, Taiyuan University of Technology, Taiyuan 030024 Shanxi, China. E-mail: lihongliang222@126.com; Prof. Xiang-Yang Lou, Institute of Technology for Future Industry (School of Science and Technology Instrument Application Engineering), Shenzhen University of Information Technology, Shenzhen 518172, Guangdong, China. E-mail: louxiangyang@sziit.edu.cn

reaction free energies, thereby accelerating reaction kinetics. Notably, the catalyst sustains stable oxygen evolution during 100 h of continuous alkaline seawater electrolysis at 50 mA cm^{-2}, and the assembled electrolyzer can additionally be driven by a commercial solar panel, demonstrating practical applicability. Overall, this work highlights transition-metal doping as a viable route for tailoring the reconstruction of MOF-derived precursors, paving the way for durable and scalable OER electrocatalysts.

INTRODUCTION

Driving electrocatalytic water splitting with renewably generated electricity provides a sustainable means of producing hydrogen. Its large-scale deployment, however, is limited by the oxygen evolution reaction (OER), whose four-electron transfer character makes the kinetics sluggish and the energy barriers intrinsically high[1,2]. Although noble-metal catalysts, particularly Ir- and Ru-based materials, exhibit excellent OER activity, their scarcity and cost have hindered industrial application[3]. As a result, research has increasingly focused on developing low-cost, earth-abundant transition-metal catalysts based on Mn, Fe, Co, and Ni[4].

Although numerous non-noble-metal OER catalysts, including metal-organic frameworks (MOFs), sulfides, and borides, have been widely reported recently, many lack stability under strongly oxidative conditions[5,6]. Rather than remaining structurally invariant during catalysis, these materials often undergo electrochemically induced surface reconstruction[7], involving ligand or anion leaching and metal oxidation to form high-valence (oxy)hydroxides that constitute the real active species[5,8]. Despite the ubiquity of dynamic transformation, research largely centers on the static properties of pristine catalysts, with limited insights into how OER-induced reconstruction governs activity. In particular, the mechanisms by which atomic doping directs structural evolution toward optimized active phases are rarely studied, limiting the rational design of high-performance catalysts.

Against this backdrop, the structurally well-defined and compositionally tunable nature of MOFs makes them valuable model precursors for sysstematically investigating how multimetallic interactions influence electrochemical reconstruction[9,10]. Among them, zeolitic imidazolate framework-67 (ZIF-67), a cobalt-based zeolitic imidazolate framework, has been widely explored for OER because of its ordered Co-N coordination environment, tunable structure, and compositional flexibility. Previous studies have improved the OER performance of ZIF-67-based catalysts through facet engineering, low-temperature deligandation to form quasi-ZIF-67, and construction of ZIF-67-derived Co-based compounds or carbon composites[11-13]. Meanwhile, *in situ* spectroelectrochemical studies have shown that ZIF-67 can reconstruct into $Co(OH)_2$/CoOOH-like species under anodic OER conditions[14], indicating that the reconstructed cobalt oxyhydroxides rather than the original Co nodes act as the dominant active sites. However, how trace heterometal incorporation regulates the reconstruction pathway of intact ZIF-67 precatalysts remains poorly understood.

Here, we report a Mn-doped ZIF-67 (Mn-ZIF-67) obtained through a facile ambient-temperature self-assembly route and systematically reveal the impact of trace Mn incorporation on the pristine catalyst and its evolution under OER conditions. Unlike previous ZIF-67-based OER studies focusing on precursor optimization or derivative design, this work targets the reconstruction process itself, using trace Mn to regulate the evolution of ZIF-67 into a Co-Mn (oxy)hydroxide active layer and establish a direct link between precursor structure, reconstruction pathway, and catalytic performance. Benefiting from earth-abundant Mn/Co elements and mild solution-phase synthesis, this system offers potential advantages in cost and scalability compared with Ir/Ru-based benchmark catalysts. Mn doping increases electrochemically accessible sites and accelerates charge-transfer kinetics, while steering *in situ* reconstruction toward a highly active Co-Mn (oxy)hydroxide phase. The resulting catalyst exhibits durable performance in alkaline seawater

splitting and is compatible with photovoltaic-powered operation. Overall, this work highlights transition-metal doping as an effective strategy for modulating MOF-based catalysts and their OER-induced reconstruction behavior, providing a rational basis for the design of efficient and robust OER electrocatalysts.

EXPERIMENTAL

Synthesis of ZIF-67 and Mn-ZIF-67

Reagents used in this study are listed in Supplementary Note 1 of the Supplementary Materials. For ZIF-67, 0.582 g of $Co(NO_3)_2·6H_2O$ was first dissolved in 30 mL of methanol, and 1.312 g of 2-methylimidazole was separately dispersed in another 20 mL of methanol; the two methanol solutions were then combined. After being stirred at ambient temperature for 1 h, the mixture was left undisturbed to age for 24 h. The resulting solid was separated by centrifugation, rinsed with methanol three times, and dried under vacuum at 65 ℃ overnight. Mn-ZIF-67 was obtained by an identical protocol, with the only difference that 0.524 g of $Co(NO_3)_2·6H_2O$ together with 0.050 g of $Mn(NO_3)_2·4H_2O$ were dissolved together in the starting 30 mL of methanol [Supplementary Figure 1]. The catalyst characterization procedures are described in Supplementary Note 2 of the Supplementary Materials.

Electrochemical measurements

Electrochemical tests were carried out on a Princeton PARSTAT MC workstation using two different configurations: a three-electrode configuration for the OER measurements in 1.0 M KOH, and a two-electrode configuration for overall seawater splitting in alkaline natural seawater. For the three-electrode measurements, catalyst-loaded nickel foam (NF, 1 cm^2) served as the working electrode, a graphite rod as the counter electrode, and an Hg/HgO electrode as the reference. The catalyst ink was prepared by ultrasonication of 5 mg of catalyst for 30 min in a solvent mixture of 450 μL ethanol, 500 μL deionized water, and 50 μL Nafion (5 wt%); 100 μL of this ink was then coated onto the pretreated NF and dried in air. After activation via 20 cyclic voltammetry (CV) cycles, linear sweep voltammetry (LSV) was conducted at 5 mV s^{-1} to evaluate OER activity. Electrochemical impedance spectroscopy (EIS) measurements were performed at 1.47 V *vs.* reversible hydrogen electrode (RHE) over a frequency range from 100 kHz to 0.01 Hz. The double-layer capacitance (C_{dl}), used to estimate the electrochemically active surface area (ECSA), was derived from non-Faradaic CV scans recorded at 40, 60, 80, 100 and 120 mV s^{-1}. Long-term stability was assessed via 12 h chronoamperometry at 1.465 V *vs.* RHE, and durability at high current density by chronopotentiometry at 1 A cm^{-2} for 24 h, using a separately prepared Mn-ZIF-67/NF electrode (1 cm^2). All potentials in the three-electrode configuration were corrected for 90% of the iR drop, with an uncompensated resistance of R_u = 0.9 Ω, and referenced to the RHE using $E_{RHE} = E_{Hg/HgO} + 0.098 + 0.059 \times pH$[15]. For the two-electrode measurements, Mn-ZIF-67/NF (1 cm^2) was used as the anode and a graphite rod as the cathode in alkaline natural seawater prepared by adding KOH to a concentration of 1.0 M to natural seawater collected from Shenzhen Bay. Details of seawater collection and electrolyte preparation are provided in Supplementary Note 3 of the Supplementary Materials, and the major-ion composition of the collected natural seawater before KOH addition is summarized in Supplementary Table 1. LSV was recorded at 5 mV s^{-1}, and long-term durability was assessed by chronopotentiometry at a constant current density of 50 mA cm^{-2} for 100 h, with deionized water periodically replenished to compensate for water consumption. Cell voltages measured in the two-electrode configuration are reported as measured, without iR correction.

Computational method

Density functional theory (DFT) computations were carried out in the Vienna *Ab Initio* Simulation Package (VASP), employing the Perdew-Burke-Ernzerhof (PBE) functional under the generalized gradient approximation (GGA)[16-18]. Interactions between ionic cores and valence electrons were treated with the projected augmented-wave (PAW) method, and the plane-wave basis set was expanded up to a kinetic energy cutoff of 450 eV[19,20]. Gaussian smearing (0.05 eV) was applied to the Kohn-Sham orbital occupancies.

To correct for strong electron correlation, Dudarev's DFT+U approach[21] was applied to the 3d electrons of Co (U_{eff} = 3.3 eV) and Mn (U_{eff} = 5.2 eV). Dispersion interactions were accounted for using Grimme's D3 dispersion correction (DFT-D3) methodology[22]. The convergence thresholds for total energy and residual force were set to 10^{-5} eV and 0.02 eV $Å^{-1}$, respectively. The Co ZIF-67 cluster was placed in a 20 Å cubic cell and fully relaxed with sampling restricted to the Γ point. For the CoOOH bulk, hexagonal lattice parameters were optimized to a = b = 2.826 Å and c = 12.936 Å. A CoOOH (001) surface model was subsequently constructed using a p (4 × 4) supercell with one stoichiometric layer and a 15 Å vacuum gap. The Mn-doped CoOOH model was constructed by substituting one Co site in the CoOOH (001) slab with Mn, and the CoOOH/Mn-doped CoOOH surfaces were used to represent the reconstructed active phases after OER activation. Structural relaxation of the slab was performed using a 2 × 2 × 1 k-point grid. Adsorption energies (E_{ads}) were calculated as follows[23]:

$$E_{\mathrm{ads}} = E_{\mathrm{A/surf}} - E_{\mathrm{surf}} - E_{\mathrm{A(\,g)}} \tag{1}$$

In this expression, $E_{A/surf}$ is the total energy after adsorption, E_{surf} is the energy of the bare slab, and $E_{A(g)}$ denotes the energy of the isolated adsorbate calculated in a 20 Å box. Free-energy corrections at 298.15 K were introduced through[23]:

$$G = E + \mathrm{ZPE} - TS \tag{2}$$

Here, E denotes the electronic energy obtained from DFT, while ZPE and S correspond to the zero-point-energy correction and entropy, respectively.

RESULTS AND DISCUSSION

Uniform rhombic dodecahedral ZIF-67 and Mn-ZIF-67 were successfully prepared via a room-temperature self-assembly method [Figure 1A-C]. Mn^{2+} incorporation modulates nucleation and suppresses crystal growth, reducing the average particle size from 0.94 ± 0.25 μm for ZIF-67 [Supplementary Figure 2] to 0.42 ± 0.09 μm for Mn-ZIF-67 [Supplementary Figure 3], which may improve electrolyte accessibility by increasing the external surface-to-volume ratio and shortening ion-diffusion pathways. Consistently, nitrogen adsorption-desorption measurements show that, although Mn-ZIF-67 has a slightly lower Brunauer-Emmett-Teller (BET) surface area than ZIF-67 (1,238.33 *vs.* 1,264.18 $m^2 g^{-1}$), its t-plot external surface area increases from 23.50 to 40.97 $m^2 g^{-1}$, accompanied by increased Barrett-Joyner-Halenda (BJH) adsorption cumulative pore area and volume from 15.49 $m^2 g^{-1}$ and 0.03025 $cm^3 g^{-1}$ to 30.96 $m^2 g^{-1}$ and 0.04332 $cm^3 g^{-1}$, respectively [Supplementary Figures 4 and 5 and Supplementary Table 2]. These results suggest enhanced external surface accessibility and mesoporous/interparticle pore contribution in Mn-ZIF-67, which are favorable for electrolyte penetration, ion transport, and anodic reconstruction. Energy-dispersive X-ray spectroscopy (EDS) mapping in Figure 1D confirms the homogeneous spatial distribution of constituent elements. Transmission electron microscopy (TEM) images retain the characteristic polyhedral outline, and the diffraction pattern recorded from an individual particle is consistent with a highly crystalline single-domain specimen (Figure 1E and inset). High-resolution TEM (HRTEM) exhibits ~ 1.21 nm lattice fringes corresponding to the ZIF-67 (011) plane [Figure 1F]. High-angle annular dark-field scanning transmission electron microscopy (HAADF-STEM) mapping likewise shows Mn and Co distributed across the same particle [Figure 1G]. Collectively, the characterization results demonstrate the incorporation of Mn^{2+} into the metal sites of the MOF without detectable formation of phase-separated Mn oxide particles.

X-ray diffraction (XRD) patterns of both ZIF-67 and Mn-ZIF-67 match the simulated patterns [Figure 2A], confirming high phase purity and preservation of the intrinsic crystal structure[24]. The absence of secondary diffraction features such as $Mn(NO_3)_2{\cdot}4H_2O$ and Mn_3O_4 further indicates the successful integration of Mn

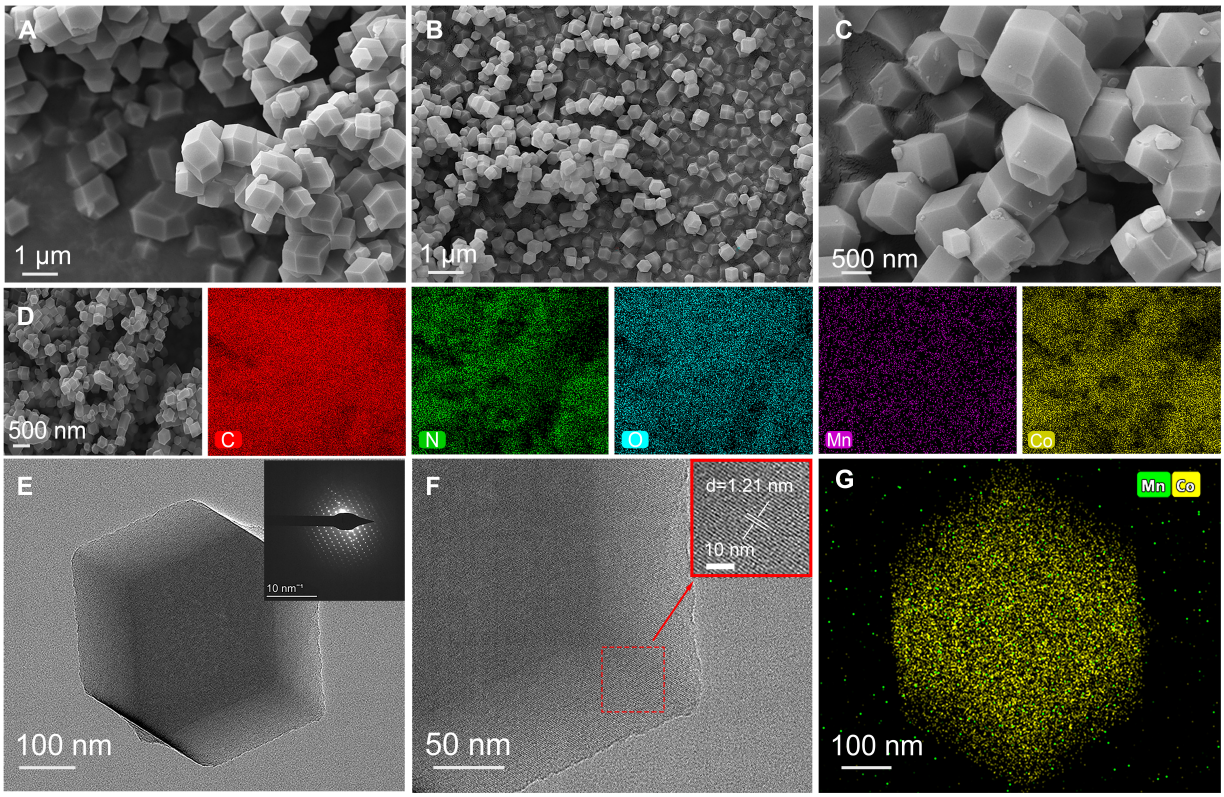

Figure 1. Microscopy of the pristine materials. (A) Scanning electron microscopy (SEM) micrograph of ZIF-67; (B and C) SEM micrographs of Mn-ZIF-67 at different magnifications; (D) Mn-ZIF-67 image and the corresponding EDS elemental maps for C, N, O, Mn and Co; all elemental maps were acquired from the same field of view and are displayed at the same spatial scale as the accompanying original image; (E) TEM micrograph with the corresponding selected-area electron diffraction (SAED) pattern in the inset; (F) HRTEM view and an enlarged lattice-fringe region; and (G) composite Mn/Co map acquired from a single Mn-ZIF-67 particle. TEM: Transmission electron microscopy; HRTEM: high-resolution transmission electron microscopy; ZIF-67: zeolitic imidazolate framework-67.

into the MOF framework without the formation of segregated impurity phases[25]. X-ray photoelectron spectroscopy (XPS) confirms the expected elemental composition of Mn-ZIF-67, including C, N, O, Co and Mn, as presented in Figure 2B[26,27]. The high-resolution N 1s spectrum in Figure 2C can be deconvoluted into metal-coordinated pyridinic nitrogen attributed to M-N bonding, where M represents Co or Mn, at approximately 398.8 eV and pyrrolic nitrogen at 400.2 eV[26]. These features confirm the coordination of 2-methylimidazole ligands and the formation of a stable ZIF-type framework[27]. To enable a more direct comparison of surface chemical states, the O 1s spectra of pristine ZIF-67 and Mn-ZIF-67 are plotted together in Figure 2D. Two main components are observed in both samples, corresponding to metal hydroxyl or adsorbed water species at 531.9 eV and to C-O species. The C-O component is located at 533.8 eV for pristine ZIF-67 and at 534.2 eV for Mn-ZIF-67, corresponding to a positive shift of 0.4 eV upon Mn incorporation. In parallel, the ratio of metal hydroxyl or adsorbed water species to C-O decreases from 4.59 to 3.28, indicating reduced surface hydroxylation and a more ligand-dominated surface environment. This result suggests that Mn incorporation modifies the local coordination environment of the pristine ZIF-67 framework. The Mn 2p spectrum in Figure 2E exhibits the characteristic Mn $2p_{3/2}$ (~ 641.2 eV) and Mn $2p_{1/2}$ (~ 652.8 eV) spin-orbit components, together with an additional satellite-related feature. It should be noted that Mn 2p spectra generally exhibit complex multiplet and final-state structures; therefore, the resolved satellite contribution is distinguished here from the Mn $2p_{3/2}$ /Mn $2p_{1/2}$ spin-orbit doublet[28]. Based on the overall spectral envelope and comparison with previously reported Mn^{2+}-containing systems, the Mn species in the as-prepared Mn-ZIF-67 are predominantly present in a Mn^{2+}-like chemical environment[29,30]. Nevertheless, considering the complex Mn 2p spectral structure and the surface-sensitive nature of XPS,

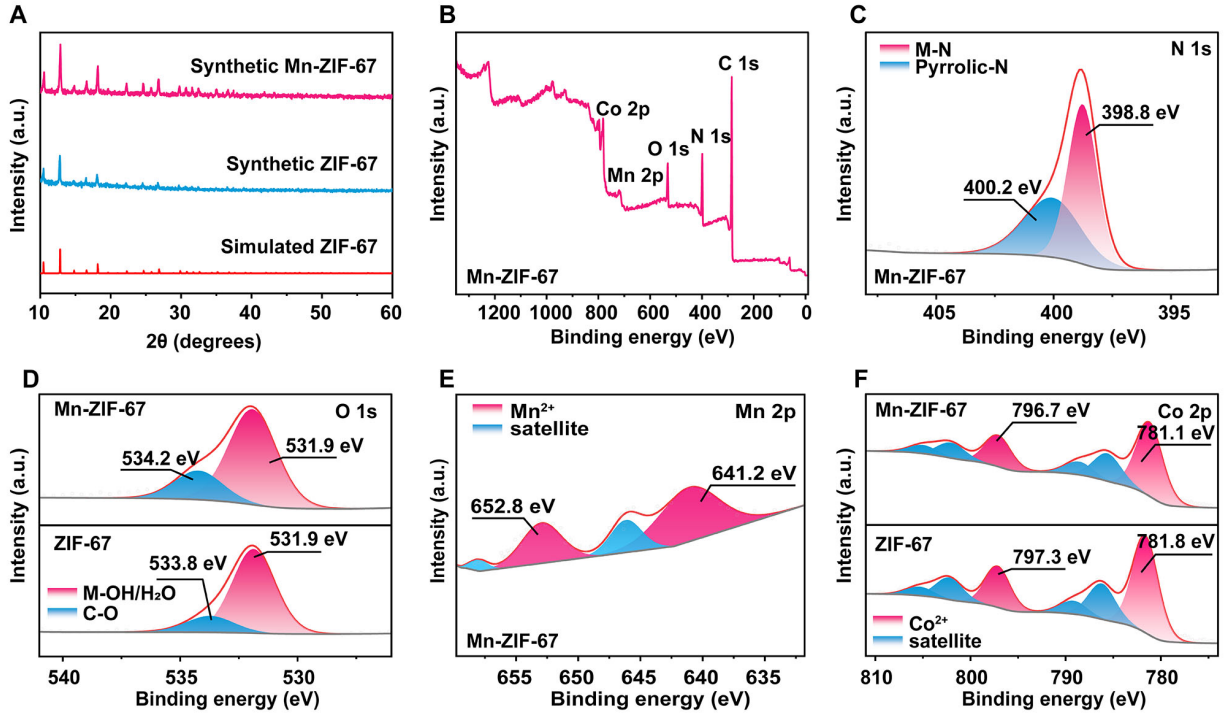

Figure 2. Structural and surface-chemical analysis of ZIF-67 and Mn-ZIF-67. (A) Experimental diffractograms ZIF-67 and Mn-ZIF-67 with the simulated ZIF-67 reference; (B) XPS spectra of Mn-ZIF-67; (C) N 1s region of Mn-ZIF-67; (D) overlaid O 1s spectra of ZIF-67 and Mn-ZIF-67; (E) Mn 2p region of Mn-ZIF-67; and (F) directly compared Co 2p spectra of ZIF-67 and Mn-ZIF-67. ZIF-67: Zeolitic imidazolate framework-67; XPS: X-ray photoelectron spectroscopy.

minor contributions from other Mn chemical states cannot be completely excluded. The directly compared Co 2p spectra of pristine ZIF-67 and Mn-ZIF-67 in Figure 2F further reveal that Mn incorporation significantly modulates the Co electronic structure. In the direct Co 2p comparison, the principal $2p_{3/2}$ feature moves by approximately 0.7 eV, from 781.8 eV for ZIF-67 to 781.1 eV after Mn introduction. This negative shift indicates increased electron density at the Co centers via the ligand-bridged framework, analogous to previously reported electron donation from boron to transition metals[31,32]. This result provides evidence of Mn-induced electronic modulation within the pristine ZIF framework, which may influence the subsequent electrochemical evolution of Mn-ZIF-67 under OER conditions.

Electrochemical OER activity was assessed in 1.0 M KOH[33]. LSV curves shown in Figure 3A reveal that both MOF-based electrodes deliver substantially higher anodic currents than the bare NF substrate, with Mn-ZIF-67 consistently outperforming ZIF-67[34]. A pre-OER anodic response appears in the 1.3-1.4 V versus RHE region. This feature is consistent with oxidation of Co species and the onset of oxyhydroxide-like reconstruction before substantial oxygen evolution[35,36]. This redox feature is more pronounced for Mn-ZIF-67, suggesting that Mn incorporation enhances the redox accessibility of Co sites and facilitates the generation of electrochemically active high-valence Co species under alkaline conditions[37]. Figure 3B displays the potentials needed to sustain the selected geometric current benchmarks. Mn-ZIF-67 requires only 235 mV to reach 10 mA cm^{-2}, 41 mV lower than ZIF-67, and maintains superior activity at 100 mA cm^{-2} with an overpotential of 310 mV compared with 353 mV for ZIF-67. An LSV backscan was further performed to exclude possible interference from Ni foam oxidation. As shown in Supplementary Figure 6, the backscan curve shows no obvious Ni oxidation peak and gives a similar overpotential at 10 mA cm^{-2}, confirming the reliable OER activity evaluation of Mn-ZIF-67. When both electrodes are compared at 1.53 V versus RHE (η = 300 mV), Mn-ZIF-67 delivers 69.8 mA cm^{-2}, versus 18.5 mA cm^{-2} for ZIF-67, corresponding to a 3.8-fold increase in geometric current response. Reaction-kinetic trends were next compared using the

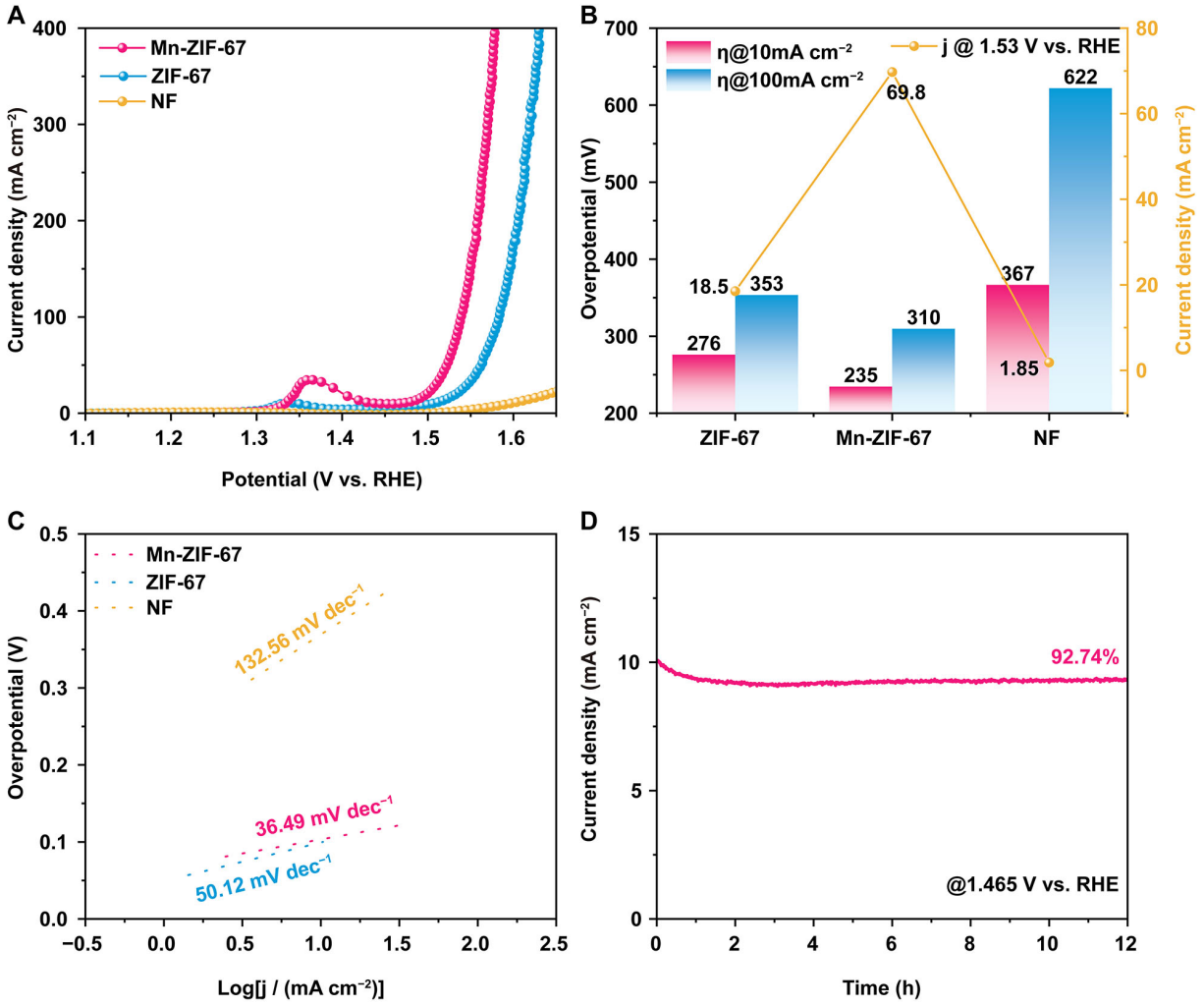

Figure 3. Alkaline OER comparison of bare NF, ZIF-67 and Mn-ZIF-67. (A) Polarization profiles recorded in 1.0 M KOH; (B) η values at 10 and 100 mA cm^{-2} together with current density at 1.53 V *vs.* RHE; (C) Tafel analysis; and (D) 12 h chronoamperometric response of Mn-ZIF-67 at 1.465 V *vs.* RHE. OER: Oxygen evolution reaction; NF: nickel foam; ZIF-67: zeolitic imidazolate framework-67; RHE: reversible hydrogen electrode.

Tafel analysis in Figure 3C. The fitted slopes are 36.49, 50.12, and 132.56 mV dec^{-1} for Mn-ZIF-67, ZIF-67, and bare NF, respectively. Combined with the lowered overpotentials, this accelerated electron transfer confirms Mn-ZIF-67 as a highly efficient alkaline OER electrocatalyst. Operational stability is a critical requirement for practical application. During the 12 h chronoamperometric test [Figure 3D], the final current remains at ~ 93% of the initial value, indicating limited activity loss over the measurement period. To further examine the durability under industrially relevant conditions, chronopotentiometry was performed at a high current density of 1 A cm^{-2} in the same three-electrode configuration. The Mn-ZIF-67 electrode sustains this current density for 24 h with the potential remaining stable at approximately 1.65 V *vs.* RHE [Supplementary Figure 7], indicating that the reconstructed active layer withstands the intense gas evolution and mechanical stress associated with high-current operation.

The origin of the distinct catalytic activity of ZIF-67 and Mn-ZIF-67 was further unraveled through combined electrochemical analysis and post-reaction characterization. Under alkaline OER conditions, the measured catalytic activity can reflect several coupled contributions, notably interfacial electron transfer, electrochemical accessibility, transport, and reconstruction of the precursor surface[38-40]. Recent studies on

water/seawater-splitting electrodes have also emphasized that reliable physicochemical characterization, including structural analysis, surface chemical-state evolution, electrochemical impedance, accessible surface-area evaluation, normalized activity comparison, and post-reaction examination, is essential for establishing meaningful structure-activity relationships[41]. Interfacial kinetic differences were first probed by EIS. As revealed by the Nyquist plots and corresponding fitting curves in Figure 4A, Mn-ZIF-67 exhibits a significantly smaller semicircle diameter than both ZIF-67 and bare NF, indicating a lower interfacial resistance under OER-relevant conditions. Quantitative fitting using an equivalent circuit model, with details provided in Supplementary Figure 8 and Supplementary Table 3, reveals that Mn-ZIF-67 possesses a low charge-transfer resistance (R_{ct}) of 2.17 Ω. This value is less than half that of ZIF-67 (4.60 Ω) and far lower than that of NF (35.36 Ω). The pronounced decrease in resistance demonstrates that Mn incorporation effectively facilitates interfacial electron transfer and reduces kinetic polarization losses during the OER process[42]. The density of electrochemically accessible active sites is another critical factor in determining catalytic activity[38]. Electrochemical accessibility was evaluated next from C_{dl} values fitted to the non-Faradaic CV data in Figure 4B and C and Supplementary Figures 9 and 10. Based on ECSA = C_{dl}/C_s, with C_s taken as 40 μF cm^{-2}, the C_{dl} values correspond to estimated ECSA values of 120.50, 63.25, and 72.50 cm^2 for Mn-ZIF-67, ZIF-67, and NF, respectively. These C_{dl}-derived ECSA values should be regarded as apparent electrochemically accessible areas rather than absolute physical surface areas, and are used here mainly for relative comparison under identical testing conditions. The larger apparent ECSA of Mn-ZIF-67 indicates more electrochemically accessible sites, which contributes to the enhanced OER performance[43]. To further evaluate the intrinsic activity of individual active sites, the LSV currents were normalized to the respective ECSA values. As displayed in Figure 4D, the ECSA-normalized polarization curves show that Mn-ZIF-67 still outperforms ZIF-67, suggesting that the improved activity is not solely caused by the increased electrochemically accessible area[44,45]. A comparison with representative ZIF-67/MOF-based and transition-metal OER electrocatalysts is summarized in Supplementary Table 4. Notably, Mn-ZIF-67 delivers a lower overpotential and Tafel slope than pristine ZIF-67 and many previously reported catalysts, highlighting its superior catalytic kinetics. The enhanced activity can be attributed to the synergistic contributions of increased electrochemically accessible surface area, accelerated interfacial charge transfer, and the formation of a Mn-containing Co oxyhydroxide-like active layer with enhanced intrinsic activity during reconstruction.

As-prepared Mn-ZIF-67 undergoes pronounced electrochemical surface reconstruction under OER conditions[46,47]. To directly monitor this structural evolution, *in situ* electrochemical Raman spectroscopy was performed under OER-relevant potentials. As shown in Figure 5A, the Raman spectra collected from open-circuit potential (OCP) to 1.80 V show clear potential-dependent changes. At lower potentials, the spectrum is dominated by Co-based oxide/oxide-like species. When the applied potential increases into the OER region, a Raman band around 503 cm^{-1} becomes more evident, which is assigned to the Co-O vibration of CoOOH. Meanwhile, the CoO_x-related band around 686 cm^{-1} evolves under anodic polarization. The potential-dependent Raman evolution therefore directly supports the formation of a CoOOH-like surface species during anodic polarization. The *in situ* Raman spectra mainly confirm the potential-induced formation of CoOOH-like species; Mn-related Raman signals are relatively weak and may overlap with Co-based vibrational features. Post-OER morphological analysis in Figure 5B shows that the initial polyhedral crystals evolve into an interconnected nanosheet architecture. Local lattice ordering in the post-OER material is visible in the HRTEM image of Figure 5C. Measured spacings of 0.193 and 0.235 nm are consistent with the reported CoOOH (104) and (101) reflections, respectively[48]. Two additional spacings, 0.262 and 0.214 nm, are consistent with values reported for MnOOH-related (-102) and (-121) planes[49]. Together with the post-OER Mn 2p evolution and inductively coupled plasma (ICP) retention data, these lattice features support the presence of Mn-containing oxyhydroxide-related regions in the reconstructed catalyst; they do not, by themselves, resolve the exact atomic arrangement of the working Mn sites[50]. XPS further clarifies the evolution of surface chemical states. The post-OER Co 2p spectra in Figure 5D show the main Co $2p_{3/2}$ peak

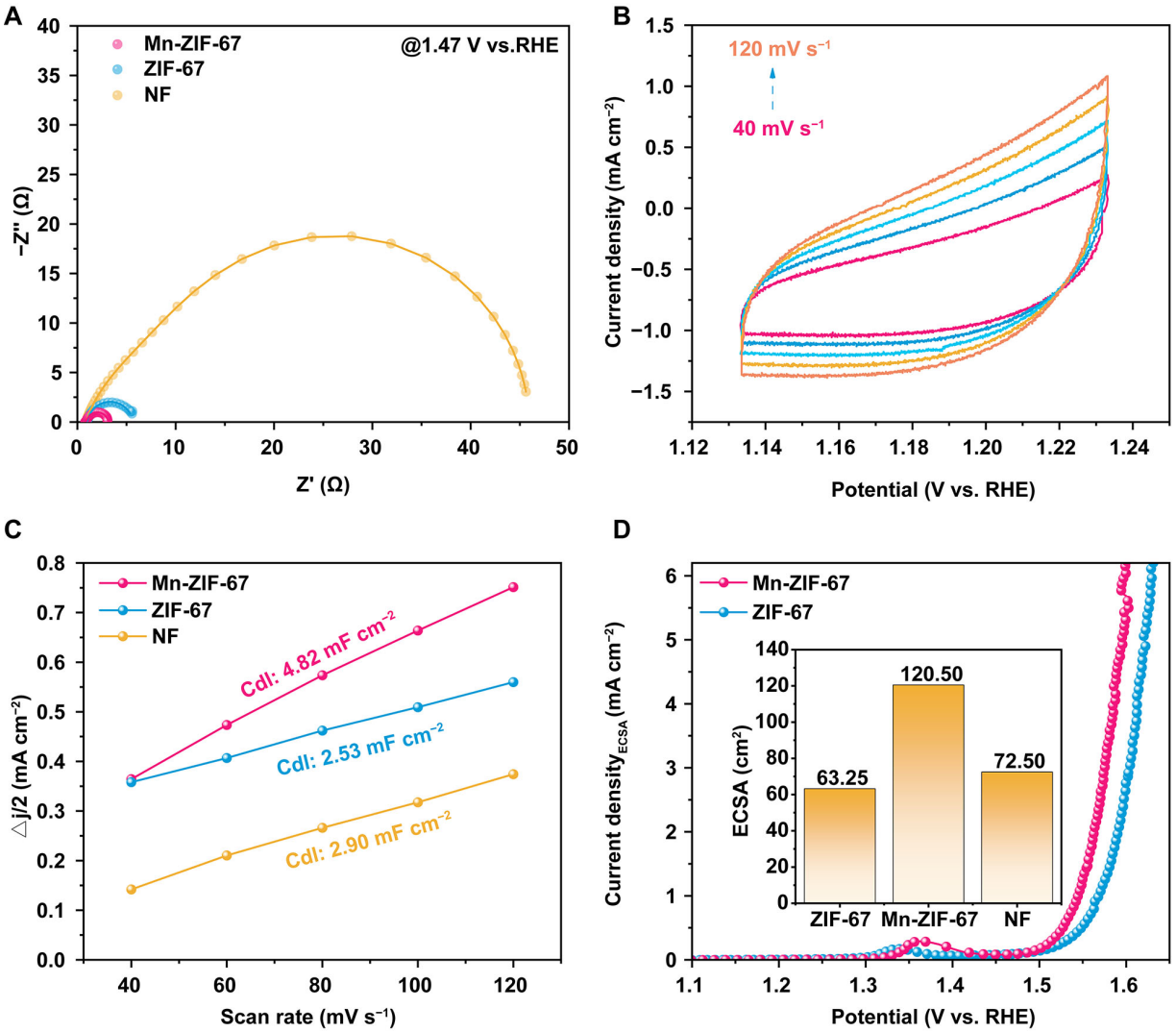

Figure 4. (A) Experimental and fitted Nyquist responses of NF, ZIF-67 and Mn-ZIF-67 at 1.47 V *vs.* RHE; (B) non-Faradaic CV series for Mn-ZIF-67; (C) linear dependence of Δj/2 on scan rate used to extract C_{dl}; and (D) ECSA-normalized polarization profiles, with estimated ECSA values shown in the inset. ZIF-67: Zeolitic imidazolate framework-67; NF: nickel foam; RHE: reversible hydrogen electrode; ECSA: electrochemically active surface area; CV: cyclic voltammetry.

shifts from 781.1 eV, characteristic of Co^{2+} with intense satellite features, to 779.9 eV with markedly suppressed satellites. This change indicates oxidation to a Co^{3+}-dominated surface, consistent with CoOOH formation[51,52]. Similarly, the post-OER Mn 2p spectra in Figure 5E show that the Mn $2p_{3/2}$ peak, initially centered at 641.2 eV and characteristic of a Mn^{2+}-like environment, shifts positively to 642.0 eV after the OER, accompanied by a marked change in line shape. This 0.8 eV positive shift and the altered line shape indicate oxidation of Mn toward a Mn^{3+}-dominated environment and support the participation of Mn in the reconstructed oxyhydroxide layer[53]. The *ex situ* XRD patterns before and after OER further show weakened diffraction features after electrolysis, indicating electrochemical reconstruction and partial loss of long-range crystallinity of the pristine ZIF framework during OER [Supplementary Figure 11]. For comparison, the post-OER surface states of pristine ZIF-67 were also examined [Supplementary Figures 12 and 13]. The post-OER Co 2p spectrum of ZIF-67 exhibits Co $2p_{3/2}$ and Co $2p_{1/2}$ peaks at 779.9 and 795.6 eV assignable to Co^{3+}-containing oxyhydroxide-like species, while the pronounced satellite features indicate that considerable Co^{2+} character remains. Meanwhile, the post-OER HRTEM image of ZIF-67 reveals lattice fringes with a spacing of 0.45 nm, corresponding to the CoOOH (003) plane, confirming that undoped ZIF-67 likewise undergoes

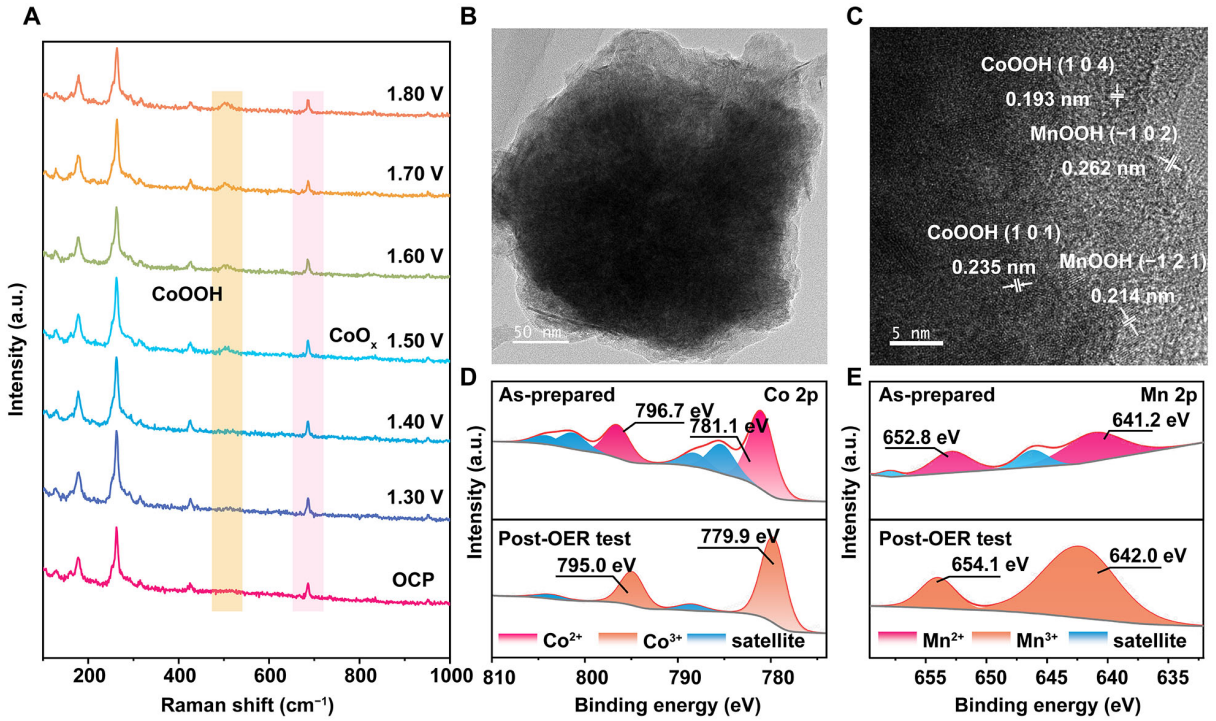

Figure 5. (A) *In situ* Raman spectra of Mn-ZIF-67 collected from OCP to 1.80 V *vs.* RHE in 1.0 M KOH. (B) TEM and (C) HRTEM images of Mn-ZIF-67 after the OER. High-resolution XPS scans of as-prepared Mn-ZIF-67 compared to the post-OER test for (D) Co 2p and (E) Mn 2p. OER: Oxygen evolution reaction; OCP: open-circuit potential; ZIF-67: zeolitic imidazolate framework-67; RHE: reversible hydrogen electrode; TEM: transmission electron microscopy; HRTEM: high-resolution transmission electron microscopy; XPS: X-ray photoelectron spectroscopy.

electrochemical reconstruction into CoOOH-like species during the OER. Compared with post-OER Mn-ZIF-67, whose Co $2p_{3/2}$ peak shifts to 779.9 eV with markedly suppressed satellites, the surface oxidation of ZIF-67 is less complete, further indicating that Mn incorporation facilitates the oxidative reconstruction of Co sites toward the active oxyhydroxide phase. To determine the actual Mn doping level and its retention after electrochemical operation, ICP analysis was performed on the catalyst-loaded electrodes before and after long-term OER operation. As summarized in Supplementary Table 5, the as-prepared Mn-ZIF-67 has an Mn/Co atomic ratio of 0.1005 ± 0.0024, close to the nominal feeding ratio of 0.111 and corresponding to an Mn incorporation efficiency of about 91%. After long-term OER operation, the ratio decreases to 0.0901 ± 0.0024, corresponding to a normalized Mn/Co atomic ratio of 89.7% of its initial value. Most Mn species are therefore retained in the reconstructed catalyst layer, consistent with the HRTEM and XPS evidence for the formation of Mn-containing oxyhydroxide species.

To obtain atomic-level insight into Mn-induced activity enhancement, DFT calculations were performed. ZIF-67 and Mn-ZIF-67 precursor models were constructed to evaluate Mn-induced charge redistribution and electronic modulation in the pristine framework [Figure 6A and B]. In addition, considering the post-OER HRTEM and XPS evidence for electrochemical reconstruction into Co/Mn oxyhydroxide species, CoOOH and Mn-doped CoOOH surface models were constructed to evaluate the OER reaction energetics on the reconstructed active surfaces [Figure 6C]. The results indicate that Mn adopts a charge state distinct from Co and induces a redistribution of electron density within the ligand-bridged ZIF framework. Although Mn and Co centers are not directly bonded in the pristine structure, the charge redistribution mediated by imidazolate linkers suggests that Mn incorporation modifies the electronic environment of the framework. This result is consistent with the Co 2p binding-energy shift observed in XPS, indicating Mn-induced electronic perturbation in the pristine Mn-ZIF-67. To further elucidate how this redistribution affects the

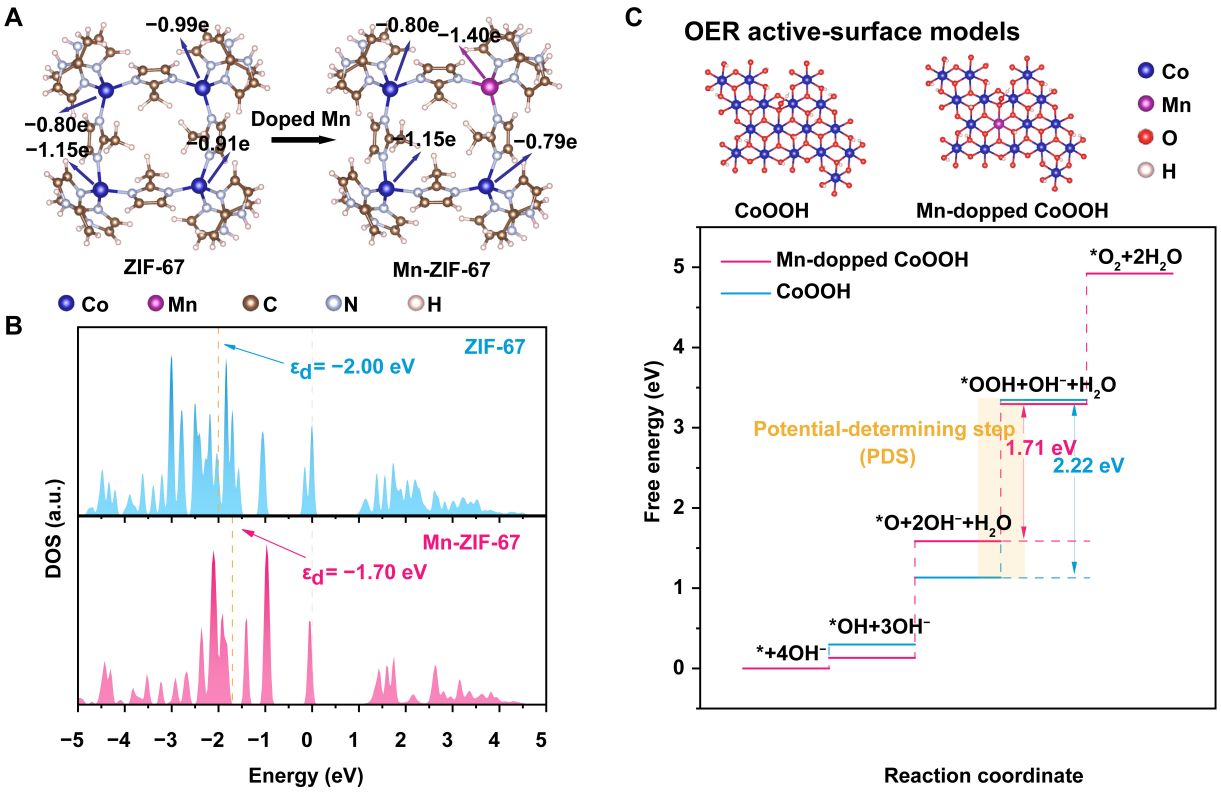

Figure 6. (A) Optimized structure models and Bader charge analysis of ZIF-67 and Mn-ZIF-67. (B) Calculated density of states and d-band centers for ZIF-67 and Mn-ZIF-67. (C) Optimized CoOOH and Mn-doped CoOOH reconstructed active-surface models and the corresponding Gibbs free-energy diagrams for the OER pathway at zero potential. OER: Oxygen evolution reaction; ZIF-67: zeolitic imidazolate framework-67.

adsorption of OER intermediates, the d-band center (ε_d) of the active metal sites was evaluated as an electronic descriptor, as shown in Figure 6B. Mn incorporation shifts ε_d upward from -2.00 eV in ZIF-67 to -1.70 eV in Mn-ZIF-67. Within the d-band framework, such an upshift of ε_d indicates stronger metal-oxygen interaction due to modified antibonding state occupancy. This effect optimizes the adsorption energetics and activation of oxygenated intermediates such as *OH, *O, and *OOH, thereby promoting OER kinetics. This trend is consistent with the experimentally observed enhancement in interfacial charge transfer and catalytic activity upon Mn incorporation.

To model the electrochemically reconstructed active surfaces suggested by post-OER characterizations, CoOOH and Mn-modified CoOOH (Mn/CoOOH) were constructed to represent the post-OER surfaces of ZIF-67 and Mn-ZIF-67, respectively[35,54,55]. The Gibbs free energy (ΔG) profiles for the four-electron OER pathway in Figure 6C show that the potenial-determining step (PDS) on CoOOH is the *O to *OOH transformation, with a ΔG of 2.22 eV. In contrast, Mn incorporation optimizes intermediate adsorption. Although the PDS remains the same, the ΔG of Mn/CoOOH decreases to 1.71 eV, significantly lowering the energetic penalty for OER turnover[56,57]. These results indicate that Mn acts as an effective electronic promoter by tuning the Co electronic structure and optimizing intermediate binding on the reconstructed oxyhydroxide surface. The free-energy profile further supports that the Mn-containing reconstructed Co oxyhydroxide surface serves as the active phase responsible for the improved OER kinetics.

To evaluate practical feasibility, a two-electrode alkaline seawater electrolyzer was assembled using a Mn-ZIF-67/Ni foam anode, a graphite rod cathode, and alkaline natural seawater collected from Shenzhen Bay[58]. When the same electrolyzer was connected to a commercial silicon solar panel, continuous gas evolution was

observed at both electrodes under natural sunlight [Figure 7A], providing qualitative proof of concept for compatibility with renewable power input[59]. The quantitative data in Figure 7B and C were acquired separately under workstation control. Overall cell performance was evaluated by LSV, as shown in Figure 7B. The Mn-ZIF-67 electrolyzer significantly outperforms the bare NF control. It delivers current densities of 10 and 50 mA cm^{-2} at 1.84 and 2.06 V, respectively, whereas the NF control requires 1.97 and 2.28 V to reach the same current densities, corresponding to reductions of 130 and 220 mV in cell voltage and indicating reduced overall-cell polarization. Chronopotentiometry measurements shown in Figure 7C further confirm excellent operational durability under harsh anodic conditions. At a constant current density of 50 mA cm^{-2}, the cell voltage remains highly stable at 2.06 V over 100 h of continuous operation without observable decay, demonstrating strong practical viability. During OER, the Mn-ZIF-67 undergoes *in situ* reconstruction into a nanosheet-like bimetallic (oxy)hydroxide layer composed of CoOOH and MnOOH nanocrystals [Figure 5C][60]. The stable operation over 100 h demonstrates the good durability of the Mn-ZIF-67-derived anode in alkaline seawater. To further examine the structural stability after seawater electrolysis, post-reaction XRD was performed. As shown in Supplementary Figure 14, the characteristic ZIF-related diffraction peaks largely disappear after electrolysis, indicating electrochemical reconstruction of the MOF precursor under anodic conditions. No crystalline chloride-containing corrosion products were detected by ex situ XRD after the test[61]. The surface chemical states after seawater electrolysis were further examined by XPS [Supplementary Figures 15 and 16]. The Co 2p spectrum of Mn-ZIF-67 after alkaline seawater electrolysis exhibits Co $2p_{3/2}$ and Co $2p_{1/2}$ peaks at 780.1 and 795.2 eV with weak satellite features, indicating that the Co^{3+}-dominated oxyhydroxide-like surface is well preserved. The Mn 2p spectrum retains well-defined Mn $2p_{3/2}$ and Mn $2p_{1/2}$ peaks at 642.3 and 654.0 eV, consistent with Mn^{3+} oxyhydroxide-like species, indicating that Mn is retained in the reconstructed layer. These chemical states closely resemble those observed after the OER in 1.0 M KOH [Figure 5D and E], further suggesting that the reconstructed Co-Mn (oxy)hydroxide layer maintains its chemical integrity against chloride attack during long-term alkaline seawater electrolysis. Collectively, these findings identify Mn-ZIF-67 as a promising anode material for solar-driven alkaline seawater electrolysis. To benchmark the overall seawater splitting performance, Mn-ZIF-67 was compared with representative ZIF/MOF-derived and Mn-containing electrocatalytic systems [Table 1]. The Mn-ZIF-67/NF || graphite rod cell requires 1.84 V at 10 mA cm^{-2} and 2.06 V at 50 mA cm^{-2} in alkaline natural seawater, showing competitive performance relative to several related systems. Together with its stable operation for 100 h at 50 mA cm^{-2} and photovoltaic-driven demonstration, these results highlight the practical potential of Mn-ZIF-67 for alkaline seawater electrolysis.

CONCLUSIONS

This work demonstrates that trace Mn doping can direct the electrochemical reconstruction pathway of ZIF-67 and thereby determine the nature of the true active phase, the OER kinetics, and the catalytic durability. Rather than acting as a static active phase, Mn-ZIF-67 behaves as a structurally dynamic catalyst under OER conditions. During anodic operation, the pristine Mn-ZIF-67 surface reconstructs into a robust bimetallic Co-Mn oxyhydroxide layer, which serves as the catalytically active phase. Density functional theory calculations confirm that Mn-induced electronic redistribution upshifts the Co d-band center, thereby lowering the Gibbs free energys of intermediates, while electrochemical measurements show that Mn incorporation simultaneously increases the density of electrochemically accessible sites and enhances interfacial charge transfer. The practical viability of this dynamically reconstructed interface is demonstrated in a two-electrode alkaline seawater electrolyzer, which sustains a current density of 50 mA cm^{-2} at approximately 2.06 V for 100 h, and which can also be operated directly using a commercial silicon solar panel. This work establishes a general mechanistic framework in which trace transition metal doping directs the *in situ* structural evolution of metal-organic frameworks, offering an effective route toward the rational design of next-generation efficient electrocatalysts.

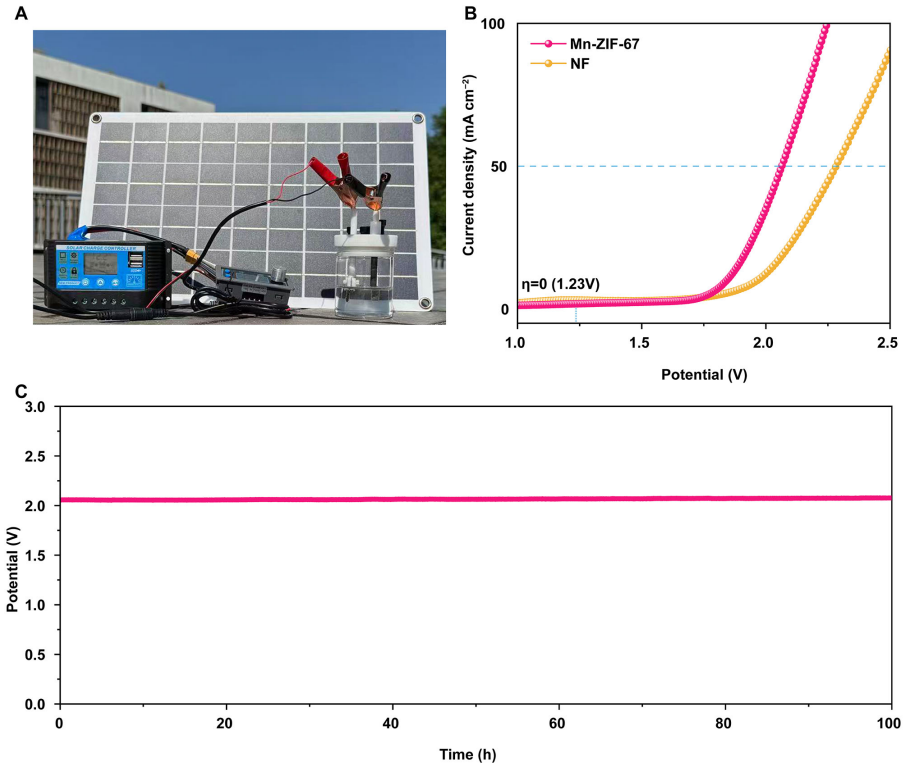

Figure 7. (A) Photograph of the assembled alkaline seawater electrolyzer connected to a commercial silicon solar panel, illustrating solar-powered operation (original photograph taken by the authors); (B) LSV of the overall seawater splitting system; (C) Chronopotentiometry analysis of Mn-ZIF-67 electrolysis for 100 h at 50 mA cm^{-2}. ZIF-67: Zeolitic imidazolate framework-67; NF: nickel foam; LSV: linear sweep voltammetry.

Table 1. Comparison of overall seawater splitting performance of Mn-ZIF-67 with representative ZIF/MOF-derived, Mn-containing, and related electrocatalytic systems

No.	Catalyst	Electrolyte	Overall seawater splitting performance	Stability	Ref.
1	Mn-ZIF-67/NF || graphite rod (this work)	1.0 M KOH + natural seawater	1.84 V at 10 mA cm^{-2}; 2.06 V at 50 mA cm^{-2}	100 h at 50 mA cm^{-2}	This work
2	ZIF-67/CF-1 || ZIF-67/CF-1	Natural seawater	2.46 V at 10 mA cm^{-2}	-	[62]
3	S-HEO/rGO-based cell	Alkaline seawater	1.85 V at 10 mA cm^{-2}	100 h at 10 mA cm^{-2}	[63]
4	Co_3Fe_1@C (Co_3Fe_1-800)-based cell	Alkaline seawater	PV-driven: 2.2 V commercial Si solar cell at 50 mA cm^{-2}	280 h at 50 mA cm^{-2}	[64]
5	NZ700 || NZ700	Alkaline seawater	1.72 V at 20 mA cm^{-2}	-	[65]
6	RhCoNi-MOF || RhCoNi-MOF	Natural alkaline seawater	1.52 V at 10 mA cm^{-2}	>80 h	[66]

ZIF-67: Zeolitic imidazolate framework-67; MOF: metal-organic framework; NF: nickel foam; CF: carbon fiber; S-HEO: spinel high-entropy oxide; rGO: reduced graphene oxide; PV: photovoltaic; NZ: Ni-exchanged ZIF-67 (NZ700 denotes pyrolysis at 700 °C).

DECLARATIONS

Authors' contributions

Conceptualization: Lou, X. Y.

Investigation, sample preparation, data curation, and formal analysis: Liu, D.; Luan, H.

Writing - original draft: Liu, D.; Li, H.; Lou, X. Y.

Writing - review and editing: Guo, H.; Li, Y.; Shao, N.; Boada, R.; Dong, Z.; Li, H.; Lou, X. Y.; Chen, Z.

Supervision: Li, H.; Lou, X. Y.; Chen, Z.

All authors discussed the results and contributed to the revision and finalization of the manuscript.

Availability of data and materials

The data supporting the findings of this study are available within the article and its Supplementary Materials. The raw datasets generated and analyzed during the current study, including the original electrochemical measurement files, XPS fitting results, XRD patterns and electron microscopy images, are available from the corresponding authors upon reasonable request.

AI and AI-assisted tools statement

Not applicable.

Financial support and sponsorship

This research was financially supported by the National Natural Science Foundation of China (52578311), Guangdong University Young Innovative Talents Program (KJ2024C034), Key Research Area Scientific Research Project (SZIIT2025KJ046), Scientific Research Start-up Fund for Doctoral and Master's Faculty (SZIIT2024KJ026), the 2025 Central Government Guidance for Local Science and Technology Development Fund Project (YDZJSX2025D092), the Fundamental Research Program of Shanxi Province (202203021221041), and the High-Level Overseas Talent Return Funding Project of the Ministry of Human Resources and Social Security (202506930038). Hanwen Luan acknowledges the financial support from the China Scholarship Council (202308440268).

Conflicts of interest

Chen, Z. serves as a Guest Editor for the Special Issue "Earth-Abundant Materials for Electrocatalytic Small Molecule Conversion" of *Energy Materials*. Chen, Z. had no involvement in the editorial processing of this manuscript, including reviewer selection, manuscript handling, or editorial decision-making. The other authors declare that they have no conflicts of interest.

Ethical approval and consent to participate

Not applicable.

Consent for publication

Not applicable.

Supplementary Materials

Supplementary Materials

REFERENCES

1. Wang, S.; Lu, A.; Zhong, C. Hydrogen production from water electrolysis: role of catalysts. *Nano. Convergence.* **2021**, *8*, 4. DOI PubMed PMC
2. Li, Z.; Wang, Y.; Lee, L. Y. S. Recent advances in synergistic modulation of transition-metal-based electrocatalysts for water oxidation: a mini review. *Catalysts.* **2023**, *13*, 1230. DOI
3. Chen, Z.; Duan, X.; Wei, W.; Wang, S.; Ni, B. Electrocatalysts for acidic oxygen evolution reaction: Achievements and perspectives. *Nano. Energy.* **2020**, *78*, 105392. DOI
4. Jannath, K. A.; Saputra, H. A. Transition metal-based electrocatalysts for alkaline oxygen evolution reaction: developments, challenges, and perspectives. *Next. Mater.* **2025**, *9*, 101164. DOI
5. Chu, H.; Li, R.; Feng, P.; et al. Ligands Defect-induced structural self-reconstruction of Fe-Ni-Co-hydroxyl oxides with crystalline/amorphous heterophase from a 2D metal-organic framework for an efficient oxygen evolution reaction. *ACS. Catal.* **2024**, *14*, 1553-66. DOI
6. Hu, Y.; Zheng, Y.; Jin, J.; et al. Understanding the sulphur-oxygen exchange process of metal sulphides prior to oxygen evolution reaction. *Nat. Commun.* **2023**, *14*, 1949. DOI PubMed PMC
7. Suresh, G.; Bang, J. H. Precatalysts: a missing link in efficient oxygen evolution electrocatalysis. *Energy. Fuels.* **2025**, *39*, 4669-92. DOI
8. Yan, P.; Liu, Q.; Zhang, H.; Qiu, L.; Wu, H. B.; Yu, X. Deeply reconstructed hierarchical and defective NiOOH/FeOOH nanoboxes with accelerated kinetics for the oxygen evolution reaction. *J. Mater. Chem. A.* **2021**, *9*, 15586-94. DOI

9. Wang, W.; Chen, D.; Li, F.; Xiao, X.; Xu, Q. Metal-organic-framework-based materials as platforms for energy applications. *Chem.* **2024**, *10*, 86-133. DOI
10. Zhang, J.; Zhu, E.; Li, R.; et al. Research progress of cobalt-based metal organic frameworks and their derivatives in energy storage and conversion. *ACS. Omega.* **2024**, *9*, 46643-63. DOI PubMed PMC
11. Zhu, R.; Ding, J.; Yang, J.; et al. Quasi-ZIF-67 for boosted oxygen evolution reaction catalytic activity via a low temperature calcination. *ACS. Appl. Mater. Interfaces.* **2020**, *12*, 25037-41. DOI
12. Wen, H.; Zhang, S.; Yu, T.; Yi, Z.; Guo, R. ZIF-67-based catalysts for oxygen evolution reaction. *Nanoscale.* **2021**, *13*, 12058-87. DOI
13. Wan, J.; Liu, D.; Xiao, H.; et al. Facet engineering in metal organic frameworks to improve their electrochemical activity for water oxidation. *Chem. Commun.* **2020**, *56*, 4316-9. DOI
14. Zheng, W.; Liu, M.; Lee, L. Y. S. Electrochemical instability of metal-organic frameworks: *in situ* spectroelectrochemical investigation of the real active sites. *ACS. Catal.* **2020**, *10*, 81-92. DOI
15. Niu, S.; Li, S.; Du, Y.; Han, X.; Xu, P. How to reliably report the overpotential of an electrocatalyst. *ACS. Energy. Lett.* **2020**, *5*, 1083-7. DOI
16. Perdew, J. P.; Burke, K.; Ernzerhof, M. Generalized gradient approximation made simple. *Phys. Rev. Lett.* **1996**, *77*, 3865-8. DOI PubMed
17. Kresse, G.; Furthmüller, J. Efficiency of *ab-initio* total energy calculations for metals and semiconductors using a plane-wave basis set. *Comput. Mater. Sci.* **1996**, *6*, 15-50. DOI
18. Kresse, G.; Furthmüller, J. Efficient iterative schemes for *ab initio* total-energy calculations using a plane-wave basis set. *Phys. Rev. B.* **1996**, *54*, 11169-86. DOI
19. Kresse, G.; Joubert, D. From ultrasoft pseudopotentials to the projector augmented-wave method. *Phys. Rev. B.* **1999**, *59*, 1758-75. DOI
20. Blöchl, P. E. Projector augmented-wave method. *Phys. Rev. B.* **1994**, *50*, 17953-79. DOI
21. Dudarev, S. L.; Botton, G. A.; Savrasov, S. Y.; Humphreys, C. J.; Sutton, A. P. Electron-energy-loss spectra and the structural stability of nickel oxide: an LSDA+U study. *Phys. Rev. B.* **1998**, *57*, 1505-9. DOI
22. Grimme, S.; Antony, J.; Ehrlich, S.; Krieg, H. A consistent and accurate *ab initio* parametrization of density functional dispersion correction (DFT-D) for the 94 elements H-Pu. *J. Chem. Phys.* **2010**, *132*, 154104. DOI PubMed
23. Nørskov, J. K.; Rossmeisl, J.; Logadottir, A.; et al. Origin of the overpotential for oxygen reduction at a fuel-cell cathode. *J. Phys. Chem. B.* **2004**, *108*, 17886-92. DOI
24. Banerjee, R.; Phan, A.; Wang, B.; et al. High-throughput synthesis of zeolitic imidazolate frameworks and application to CO_2 capture. *Science.* **2008**, *319*, 939-43. DOI
25. Xing, L.; Liu, J.; Qi, T.; Wang, L.; Wang, Z.; Zhang, S. Superior energy-saving catalyst of Mn@ZIF67 for reclaiming byproduct in wet magnesia desulfurization. *App. Catal. B:. Environ.* **2020**, *275*, 119143. DOI
26. Saeidi, M.; Amidian, M. A.; Sheybanikashani, S.; et al. Multilayered mesoporous composite nanostructures for highly sensitive label-free quantification of cardiac troponin-I. *Biosensors.* **2022**, *12*, 337. DOI PubMed PMC
27. Nie, L.; Yang, Y.; Xin, S.; Fang, C.; Chen, H.; Kang, N. Easy-regeneration Mn-doped ZIF-67 derivate adsorbent with ultra-high adsorption capacity for tetracycline hydrochloride in wastewater. *Sep. Purif. Technol.* **2024**, *338*, 126429. DOI
28. Biesinger, M. C.; Payne, B. P.; Grosvenor, A. P.; Lau, L. W.; Gerson, A. R.; Smart, R. S. Resolving surface chemical states in XPS analysis of first row transition metals, oxides and hydroxides: Cr, Mn, Fe, Co and Ni. *Appl. Surf. Sci.* **2011**, *257*, 2717-30. DOI
29. Bakar, B.; Dik, G.; Ulu, A.; Ateş, B. Immobilization of xylanase into zeolitic imidazolate framework-67 (ZIF-67) and manganese-doped ZIF-67 (Mn/ZIF-67): a comparison study. *Top. Catal.* **2024**, *67*, 698-713. DOI
30. Chen, Z.; Zou, W.; Zheng, R.; et al. Synergistic recycling and conversion of spent Li-ion battery leachate into highly efficient oxygen evolution catalysts. *Green. Chem.* **2021**, *23*, 6538-47. DOI
31. Liu, X.; Liu, H.; He, G.; Zhu, Y.; Xiao, J.; Han, L. Borate anion dopant inducing oxygen vacancies over Co_3O_4 nanocages for enhanced oxygen evolution. *Catalysts.* **2021**, *11*, 659. DOI
32. Wu, Z.; Gao, J.; Kuang, Y. Non-metallic doping of multinary metal oxide semiconductors for energy applications. *Catalysts.* **2025**, *15*, 1062. DOI
33. Chen, Z.; Zheng, R.; Wei, W.; Wei, W.; Ni, B.; Chen, H. Unlocking the electrocatalytic activity of natural chalcopyrite using mechanochemistry. *J. Energy. Chem.* **2022**, *68*, 275-83. DOI
34. Selvasundarasekar, S. S.; Bijoy, T. K.; Kumaravel, S.; et al. Effective formation of a Mn-ZIF-67 nanofibrous network via electrospinning: an active electrocatalyst for OER in alkaline medium. *ACS. Appl. Mater. Interfaces.* **2022**, *14*, 46581-94. DOI
35. Lee, W. H.; Han, M. H.; Ko, Y.; Min, B. K.; Chae, K. H.; Oh, H. Electrode reconstruction strategy for oxygen evolution reaction: maintaining Fe-CoOOH phase with intermediate-spin state during electrolysis. *Nat. Commun.* **2022**, *13*, 605. DOI PubMed PMC
36. Zhong, H.; Zhang, Q.; Yu, J.; et al. Fundamental understanding of structural reconstruction behaviors in oxygen evolution reaction electrocatalysts. *Adv. Energy. Mater.* **2023**, *13*, 2301391. DOI

37. Raj, S.; Anantharaj, S.; Kundu, S.; Roy, P. *In situ* Mn-doping-promoted conversion of $Co(OH)_2$ to Co_3O_4 as an active electrocatalyst for oxygen evolution reaction. *ACS. Sustainable. Chem. Eng.* **2019**, *7*, 9690-8. DOI
38. Wei, C.; Sun, S.; Mandler, D.; Wang, X.; Qiao, S. Z.; Xu, Z. J. Approaches for measuring the surface areas of metal oxide electrocatalysts for determining their intrinsic electrocatalytic activity. *Chem. Soc. Rev.* **2019**, *48*, 2518-34. DOI
39. Anantharaj, S.; Kundu, S. Do the evaluation parameters reflect intrinsic activity of electrocatalysts in electrochemical water splitting? *ACS. Energy. Lett.* **2019**, *4*, 1260-4. DOI
40. Bakovic, S. I.; Acharya, P.; Watkins, M.; Thornton, H.; Hou, S.; Greenlee, L. F. Electrochemically active surface area controls HER activity for Fe_xNi_{100-x} films in alkaline electrolyte. *J. Catal.* **2021**, *394*, 104-12. DOI
41. Muthurasu, A.; Ko, T. H.; Kim, T. W.; Chhetri, K.; Kim, H. Y. Interfacial electronic modification of nickel phosphide via iron doping: an efficient bifunctional catalyst for water/seawater splitting. *Adv. Funct. Mater.* **2024**, *34*, 2404254. DOI
42. Liu, S.; Shuai, Y.; Zhang, T.; Liu, X.; Ding, Z.; Liu, Y. Optimizing charge pathways by interface engineering in $Fe_2O_3/Co_3O_4/Co(PO_3)_2$ heterostructures for superior oxygen evolution reaction. *Sci. Rep.* **2025**, *15*, 7025. DOI PubMed PMC
43. Connor, P.; Schuch, J.; Kaiser, B.; Jaegermann, W. The determination of electrochemical active surface area and specific capacity revisited for the system MnO_x as an oxygen evolution catalyst. *Z. Phys. Chem.* **2020**, *234*, 979-94. DOI
44. Dionigi, F.; Zhu, J.; Zeng, Z.; et al. Intrinsic electrocatalytic activity for oxygen evolution of crystalline 3d-transition metal layered double hydroxides. *Angew. Chem. Int. Ed.* **2021**, *60*, 14446-57. DOI PubMed PMC
45. Jeon, S. S.; Kang, P. W.; Klingenhof, M.; Lee, H.; Dionigi, F.; Strasser, P. Active surface area and intrinsic catalytic oxygen evolution reactivity of NiFe LDH at reactive electrode potentials using capacitances. *ACS. Catal.* **2023**, *13*, 1186-96. DOI
46. He, B.; Bai, F.; Jain, P.; Li, T. A review of surface reconstruction and transformation of 3d transition-metal (oxy)hydroxides and spinel-type oxides during the oxygen evolution reaction. *Small.* **2025**, *21*, 2411479. DOI PubMed PMC
47. Wu, Q.; Wang, S.; Guo, J.; et al. Insight into sulfur and iron effect of binary nickel-iron sulfide on oxygen evolution reaction. *Nano. Res.* **2022**, *15*, 1901-8. DOI
48. Kudielka, A.; Bette, S.; Dinnebier, R. E.; Abeykoon, M.; Pietzonka, C.; Harbrecht, B. Variability of composition and structural disorder of nanocrystalline CoOOH materials. *J. Mater. Chem. C.* **2017**, *5*, 2899-909. DOI
49. Kohler, T.; Armbruster, T.; Libowitzky, E. Hydrogen bonding and Jahn-Teller distortion in groutite, α-MnOOH, and manganite, γ-MnOOH, and their relations to the manganese dioxides ramsdellite and pyrolusite. *J. Solid. State. Chem.* **1997**, *133*, 486-500. DOI
50. Wang, S.; Jiang, Q.; Ju, S.; et al. Identifying the geometric catalytic active sites of crystalline cobalt oxyhydroxides for oxygen evolution reaction. *Nat. Commun.* **2022**, *13*, 6650. DOI PubMed PMC
51. Shamraiz, U.; Majeed, A.; Raza, B.; Ain, N. U.; Badshah, A. Exploring the potential of cobalt hydroxide and its derivatives as a cost-effective and abundant alternative to noble metal electrocatalysts in oxygen evolution reactions: a review. *Sustain. Energ. Fuels.* **2024**, *8*, 422-59. DOI
52. Liu, Y.; Koza, J. A.; Switzer, J. A. Conversion of electrodeposited $Co(OH)_2$ to CoOOH and Co_3O_4, and comparison of their catalytic activity for the oxygen evolution reaction. *Electrochim. Acta.* **2014**, *140*, 359-65. DOI
53. Ramírez, A.; Hillebrand, P.; Stellmach, D.; May, M. M.; Bogdanoff, P.; Fiechter, S. Evaluation of MnO_x, Mn_2O_3, and Mn_3O_4 electrodeposited films for the oxygen evolution reaction of water. *J. Phys. Chem. C.* **2014**, *118*, 14073-81. DOI
54. Bajdich, M.; García-mota, M.; Vojvodic, A.; Nørskov, J. K.; Bell, A. T. Theoretical investigation of the activity of cobalt oxides for the electrochemical oxidation of water. *J. Am. Chem. Soc.* **2013**, *135*, 13521-30. DOI
55. Chen, Z.; Cai, W.; Zhang, H.; Xiao, K.; Huang, B.; Liu, Z. Spin polarization induced rapid reconstruction of transition metal oxide for efficient water electrolysis. *Chem. Sci.* **2025**, *16*, 14750-9. DOI PubMed PMC
56. Rossmeisl, J.; Qu, Z.; Zhu, H.; Kroes, G.; Nørskov, J. Electrolysis of water on oxide surfaces. *J. Electroanal. Chem.* **2007**, *607*, 83-9. DOI
57. Rossmeisl, J.; Logadottir, A.; Nørskov, J. Electrolysis of water on (oxidized) metal surfaces. *Chem. Phys.* **2005**, *319*, 178-84. DOI
58. Pal, M.; Biswas, R.; Trivedi, V.; Saini, A.; Dutta, A. Green hydrogen production by alkaline seawater electrolyzers: a transition from lab-scale research to industrial-scale applications. *J. Mater. Chem. A.* **2026**, *14*, 6106-44. DOI
59. Zhang, Q.; Shan, Y.; Pan, J.; et al. A photovoltaic-electrolysis system with high solar-to-hydrogen efficiency under practical current densities. *Sci. Adv.* **2025**, *11*, eads0836. DOI PubMed PMC
60. Li, S.; Wang, K.; Liang, C.; et al. Growth of superhydrophilic metal-oxyhydroxide layer as “firebreak forest” for exponentially enhanced stability in seawater splitting. *Chem. Catalysis.* **2023**, *3*, 100789. DOI
61. Zhang, S.; Wang, Y.; Li, S.; et al. Concerning the stability of seawater electrolysis: a corrosion mechanism study of halide on Ni-based anode. *Nat. Commun.* **2023**, *14*, 4822. DOI PubMed PMC
62. Chen, Y.; Zhao, X.; Zhang, Q.; et al. Carbon fiber supported Co/Co_3O_4-embedded N-doped carbon microparticles for efficient overall seawater splitting and oxygen reduction. *Int. J. Hydrogen. Energy.* **2023**, *48*, 3759-67. DOI

63. Sarma, Y. S. S.; Ghosh, A.; Jaiswal, M.; Bhattacharya, S.; Ramaprabhu, S. A spinel based high entropy oxide (Co, Fe, Mn, Ni, Li)$_3$O$_4$ and reduced graphene oxide composite anode for seawater electrolysis. *Int. J. Hydrogen. Energy.* **2025**, *130*, 54-63. DOI
64. Jiang, Q.; Chen, Z.; Bai, M.; et al. Upcycling of waste polyethylene terephthalate (PET) into CoFe@C for highly efficient PV-driven bifunctional seawater splitting via a "waste materialization" strategy. *Appl. Catal. B. Environ.* **2025**, *362*, 124756. DOI
65. Fathima, T. S.; Ghosh, A.; Ramaprabhu, S. Efficient, chlorine-free, and durable alkaline seawater electrolysis enabled by MOF-derived nanocatalysts. *Int. J. Hydrogen. Energy.* **2024**, *90*, 546-56. DOI
66. Tran, N. Q.; Truong, T. T.; Tran, T. T. N.; et al. Multi-metallic metal-organic framework nanosheets with 3D flower-like nanostructure-based natural seawater splitting toward stable industrial-scale current density. *ACS. Sustainable. Chem. Eng.* **2024**, *12*, 1038-50. DOI